10.24425/acs.2023.146961

Archives of Control Sciences
Volume 33(LXIX), 2023
No. 3, *pages 589–606*

ARL-Wavelet-BPF optimization using PSO algorithm for bearing fault diagnosis

Muhammad AHSAN, Dariusz BISMOR and Muhammad Arslan MANZOOR

Rotating element bearings are the backbone of every rotating machine. Vibration signals measured from these bearings are used to diagnose the health of the machine, but when the signal-to-noise ratio is low, it is challenging to diagnose the fault frequency. In this paper, a new method is proposed to enhance the signal-to-noise ratio by applying the Asymmetric Real Laplace wavelet Bandpass Filter (ARL-wavelet-BPF). The Gaussian function of the ARL-wavelet represents an excellent BPF with smooth edges which helps to minimize the ripple effects. The bandwidth and center frequency of the ARL-wavelet-BPF are optimized using the Particle Swarm Optimization (PSO) algorithm. Spectral kurtosis (SK) of the envelope spectrum is employed as a fitness function for the PSO algorithm which helps to track the periodic spikes generated by the fault frequency in the vibration signal. To validate the performance of the ARL-wavelet-BPF, different vibration signals with low signal-to-noise ratio are used and faults are diagnosed.

Key words: signal-to-noise ratio, asymmetric real Laplace wavelet, bandpass filter, particle swarm optimization, spectral kurtosis, fault frequency.

1. Introduction

The vibration signal measured from a rotating element bearing contains a background noise which results in decreasing the signal-to-noise ratio. When a fault occurs in the bearing, the power of the fault frequency is very low in the beginning. The power then exponentially increases and the rotating element bearing finally gets damaged. Therefore, it is crucial to diagnose the faults in their early stages to save the rotating machines from the sudden shutdown, which

M. Ahsan (corresponding author, e-mails: ahsanmuhammad@aol.com, Muhammad.Ahsan@polsl.pl) and D. Bismor are with Department of Measurements and Control Systems, Silesian University of Technology, 44-100 Gliwice, Poland.

M.A. Manzoor is with Department of Natural Language Processing, Mohamed bin Zayed University of Artificial Intelligence, Abu Dhabi, UAE.

Received 26.01.2023. Revised 11.06.2023.

causes both financial and health problems [7,17]. In [13], a mixed H_2/H_∞ control design is proposed for the augmented observer-based fault estimation.

The faults in rotating element bearings produce a periodic impact in the vibration signal which can be diagnosed using different signal processing techniques in the time-domain, the frequency-domain, and the time-frequency-domain [16]. Health diagnosis of the rotating element bearing means to determine these periodic impulses and if the vibration signal has these periodic impulses, take the necessary steps for predictive maintenance. But this is a challenging task because of the low signal-to-noise ratio and hence traditional methods fail to diagnose the faults.

The following equation represents the periodic impulses in frequency-domain representation:

$$S_f = \sum_k X_k h(t - \tau_k), \tag{1}$$

where X_k is the Fourier transform of the time-domain vibration signal $x(t)$ and $h(t)$ represents the impulse response with random time of the impacts τ_k and a random sequence of amplitudes X_k. k is the set of real numbers. The rolling elements of a bearing possess random slips and random pulses, and hence it is known as a stochastic process. The resulting signals are pseudo-cyclostationary instead of cyclostationary due to the lack of memory of the previous slips but are usually treated as cyclostationary [15,20].

It is important to increase the signal-to-noise ratio of the faulty signal before applying signal processing techniques and for that, a bandpass filter (BPF) can be applied which enhances the signal power, and then the faults are easily diagnosed. In the literature, different techniques are used to find the faults in rotating element bearing such as envelope spectrum, kurtosis, spectral kurtosis (SK), and so on [11,22].

Antoni [4,6] proposed a kurtogram using the SK to detect the frequency location of non-stationary transients in vibration signals and then further enhanced the performance of the kurtogram by introducing the fast kurtogram in which binary tree was employed to design the BPF [5]. In literature, the fast kurtogram was used by many researchers to diagnose the faults in rotating element bearings [10,12]. However, the BPF constructed using the fast kurtogram has constant bandwidth and center frequency because the binary tree divides the frequency spectrums at the specific frequency. Therefore, it is highly possible that the constructed BPF using a fast kurtogram possesses diverted bandwidth and center frequency from the fault frequency spectrum. To solve optimized bandwidth and center frequency problems, optimization methods such as the harmony search (HS) algorithm are also employed [2,3]. Another problem with the fast kurtogram is that it uses the kurtosis of the time-domain signal. The kurtosis fails to determine the periodicity

in the signal because its value depends on the spikes in the signal which could be due to noise. Wang [23] employed the kurtosis based on the envelope spectrum of the signal and proposed an enhanced kurtogram. But similar to the binary tree, in an enhanced kurtogram, the vibration signal is decomposed to different depths that result in a bank of different filters. In [14], the wavelet packet transform (WPT) is used to divide the frequency band and the bank of BPF is constructed. In [19], a fast neural network and genetic algorithm are used to design the smooth orthogonal wavelet.

The continuous wavelet transform (CWT) efficiently divides the frequencies of the vibration signal [21, 24] by producing different filters possessing different bandwidths and center frequencies. In this process, the mother wavelet of a specific wavelet basis function is stretched and translated. The fault frequency is diagnosed using the produced filters but for that, the parameters of the wavelet are selected precisely. There are two challenges in the CWT method, the first one is the selection of step size for bandwidth and center frequency, and the second one is the computational time to determine a suitable filter.

Motivated by the aforementioned literature review, this paper proposes an alternative approach to design the BPF for fault diagnosis for low signal-to-noise ratio vibration signals. In the proposed approach, a bank of different BPF is not required, thus lowering the computational time. The center frequency and bandwidth of the BPF are optimized using an optimization algorithm. The main contributions of this paper include:

- Involvement of the Asymmetric Real Laplace (ARL) wavelet as the wavelet base function to construct the CWT and diagnose the fault frequency. The ARL-wavelet is more efficient than the Morlet wavelet for vibration fault diagnosis due to its asymmetric geometric shape.

- Optimization of the bandwidth and center frequency of the CWT-wavelet-BPF using the Particle Swarm Optimization (PSO) algorithm. The PSO algorithm minimizes the computational time and filters bank is not required to construct.

- Use of the SK of the envelope spectrum of vibration signal as the fitness function to evaluate the strength of the fault frequency in the filtered signal.

The rest of the paper is organized as follows: Section 2 consists of ARL-wavelet-BPF in which the model of the proposed filter is constructed. Section 3 discusses the fitness function. Section 4 presents the PSO algorithm and its main steps for the implementation of the optimization problem. Section 5 shows the results of the proposed method for different vibration signals having low signal-to-noise ratios.

2. Asymmetric real Laplace wavelet bandpass filter

The continuous wavelet transform $W(\alpha, \beta)$ of a signal $x(t)$ is given by [18]:

$$W(\alpha, \beta) = |\alpha|^{1/2} \int_{-\infty}^{+\infty} x(t) \phi^* \left(\frac{t - \beta}{\alpha} \right) \mathrm{d}t, \tag{2}$$

where α and β represent scale and shift parameters, respectively; $\phi(.)$ is wavelet function; and $*$ shows the conjugate. In the frequency domain, it can be written as follow:

$$W(\alpha, \beta) = |\alpha|^{1/2} IFT \left[X(f) \psi^*(\alpha f) \right], \tag{3}$$

where $X(f)$ and $\psi(f)$ are the Fourier transform of the signal and wavelet function, respectively; and IFT represents the inverse Fourier transform.

The wavelet function in Equation (2) is composed of a sine wave with a Gaussian function. This sine wave could be real or complex. For ARL-wavelet the sine wave is a real sine function with the frequency f_c. The wavelet function $\phi(t)$ for ARL-wavelet filter can be written as follow:

$$\phi(t) = \exp(-\pi\sigma|t|) \sin(2\pi f_c t), \tag{4}$$

where f_c and σ represent the center frequency and bandwidth of the ARL-wavelet-BPF. In the frequency domain, it can be written as follow:

$$\psi(f) = \frac{\sigma}{j\pi \left[\sigma^2 + 4(f - f_c)^2 \right]} - \frac{\sigma}{j\pi \left[\sigma^2 + 4(f + f_c)^2 \right]}. \tag{5}$$

Fig. 1 shows the ARL-wavelet in the time and frequency domains. The shape of the Gaussian function depends on the σ which is also known as the "number of cycles" or the bandwidth of the Gaussian function. A wider Gaussian function leads to an increase of the spectral precision and decrease of the temporal precision. In the same time, the center frequency f_c is also important for the optimized BPF such that it could detect the fault frequency. In Fig. 1a and 1b, the center frequency f_c is 20 Hz, and the bandwidth σ is 5 Hz. When the bandwidth is increased to 10 Hz as shown in Fig. 1c and 1d, the spectral precision is increased.

The ARL-wavelet is an efficient BPF for vibration signals due to many reasons such as:

- In the frequency-domain, the ARL-wavelet has a Gaussian shape and smooth edges help to minimize the ripple effects.
- The ARL-wavelet convolution with a vibration signal retains the temporal resolution of the original signal.

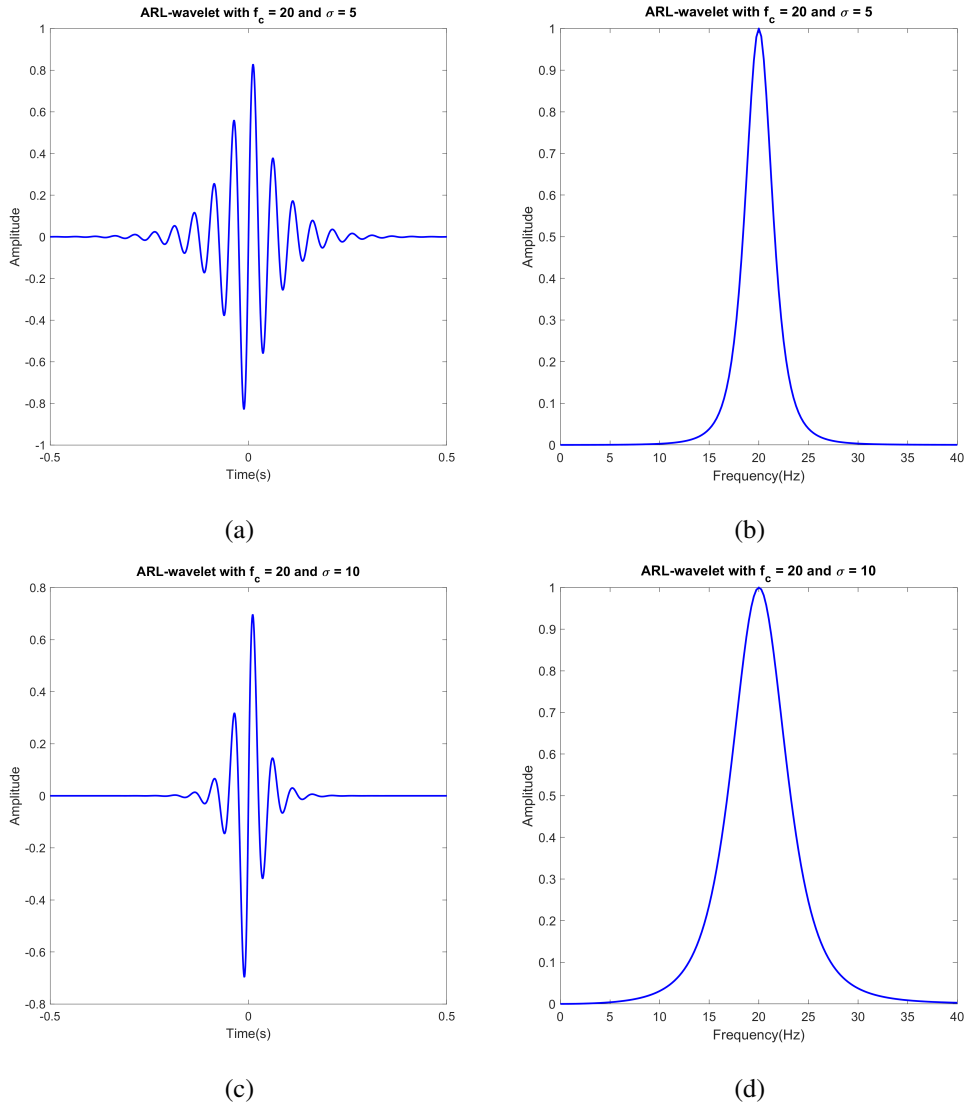

Figure 1: ARL-wavelet: a) time plot with $f_c = 20$ and $\sigma = 5$, b) frequency plot with $f_c = 20$ and $\sigma = 5$, c) time plot with $f_c = 20$ and $\sigma = 10$, d) frequency plot with $f_c = 20$ and $\sigma = 10$

- The computational time and complexity are small for the ARL-wavelet convolution with vibration signal.

The convolution of the vibration signal and the ARL-wavelet can be written as follow:

$$W_x(f_c, \sigma) = IFT\left[X(f)\psi^*(f)\right]. \tag{6}$$

The bandwidth and center frequency of the ARL-wavelet-BPF must be selected carefully to diagnose the fault frequency in the rotating element bearing. Because of the unknown noise and fault frequency, it is challenging to find these parameters. Therefore, the PSO optimization algorithm with SK of the envelope spectrum of the vibration signal is employed in this paper to estimate these parameters.

3. Fitness function

The strength of the spikes in the vibration signal can be measured using the kurtosis and hence it is an effective indicator to determine the fault frequency components in rotating element bearing. For a vibration signal $x(t)$ with N number of samples, the kurtosis is defined as the expected value of the fourth power of the random signal $x(t)$ centralized using the mean and standardized using the standard derivative and is defined as follow:

$$K = \frac{\frac{1}{N}\sum_{i=1}^{N}(x_i(t) - \bar{x}(t))^4}{\left(\frac{1}{N}\sum_{i=1}^{N}(x_i(t) - \bar{x}(t))^2\right)^2}. \tag{7}$$

In the equation (7), $\bar{x}(t)$ is the mean of the N samples.

The kurtosis is measured over the whole frequency band whereas SK is measured over each frequency band and hence is more effective to track the hidden transients. Antoni in [4, 6] applied the signal and system theory to represent the SK as the fourth-order spectral cumulant and it can be represented as follow:

$$K_x(f) = \frac{\langle X^4(t,f)\rangle}{\langle X^2(t,f)\rangle^2} - 2, \tag{8}$$

where $\langle . \rangle$ represents the time averaging operator, and $X(t,f)$ is the time-frequency envelope spectrum of the vibration signal $x(t)$. $X(t,f)$ is a complex envelope that is associated with the vibration signal $x(t)$ as follows:

$$x(t) = \int_{+1/2}^{-1/2} X(t,f)e^{j2\pi ft}\,\mathrm{d}Z_t(f). \tag{9}$$

The following equation represents the SK formula for a non-stationary vibration signal subjected to noise $n(t)$:

$$K_{x+n}(f) = \frac{K_x(f)}{[1+\rho(f)]^2}, \tag{10}$$

where $\rho(f)$ is the function of frequency representing the noise-to-signal ratio. In this paper, the SK of the envelope spectrum of the vibration signal is used as the fitness function because it is an excellent indexing tool to determine the periodic spikes in the vibration signal.

4. The PSO algorithm

The PSO algorithm [9, 25] consists of m number of particles (the swarm size), and each particle is considered as the potential solution of the complex problem. Each particle $i \in \{1, 2, 3, \ldots, k\}$ has position $P = [p_{m1}, p_{m2}, \ldots, p_{mD}]$ and velocity $V = [v_{m1}, v_{m2}, \ldots, v_{mD}]$ vectors of D-dimension, where D is the number of variables to be optimized in the search space. During the optimization process, the flight trajectory of the particles moves toward the optimized solution. The vectors P and V are said to be the candidate solution of the optimization problem and search direction, respectively. At each epoch, the PSO algorithm updates position and velocity vectors using the following relations:

$$\begin{aligned} v_{md}(k+1) &= W v_{md}(k) + c_1 r_1 \left(p_{\text{best}}(k) - p_{md}(k)\right) \\ &\quad + c_2 r_2 \left(g_{\text{best}}(k) - p_{md}(k)\right), \\ p_{md}(k+1) &= p_{md}(k) + v_{md}(k+1), \end{aligned} \tag{11}$$

where k is the number of epochs; W is the inertia weight associated with the previous velocity preservation; r_1 and r_2 are two random numbers in the interval $[0 \quad 1]$; c_1 and c_2 are two acceleration coefficients determining the relative learning weights for p_{best} and g_{best}. $p_{md}(k)$ and $v_{md}(k)$ are the position and velocity of the m-th particle, d-th dimension at k-th epoch, respectively. Moreover, $P_{\text{best}} = [p_{\text{best}}(1), p_{\text{best}}(2), \ldots, p_{\text{best}}(k)]$ is the particle best solution within each epoch also known as a historical best population while $G_{\text{best}} = [g_{\text{best}}(1), g_{\text{best}}(2), \ldots, g_{\text{best}}(k)]$ is the global best solution after each epoch.

Generally, the PSO algorithm is divided into the following steps:

Step 1: In step 1, the fitness function is defined. In this paper, the SK of the envelope spectrum of the vibration signal is utilized as a fitness function. The value of the proposed fitness function varies with the fault frequency strength. The strength of the spikes representing fault frequency improves if the signal-to-noise ratio is enhanced. Consequently, the value of the fitness function increases and faults are diagnosed.

Step 2: In step 2, the parameters of the PSO algorithm are defined. Table 1 includes these parameters.

The lower bound and the upper bound of the variables (bandwidth and center frequency) depends on fault types. The lower bound and upper bound for

Table 1: Parameters of PSO algorithm

Variable	Value	Description
D	2	number of variables
m	50	swarm size
c_1	1.25	acceleration factor
c_2	1.75	acceleration factor
$w_{\min}$	0.5	minimum inertia weight
$w_{\max}$	0.9	maximum inertia weight
s_{lb}	–	lower bound of variables
s_{ub}	–	upper bound of variables
epoch	50	total number of epoch

bandwidth are given by $[\sigma_{lb} \;\; \sigma_{ub}] = [2f_f \;\; \frac{1}{2}f_s]$ and for the center frequency, $[f_{clb} \;\; f_{cub}] = [f_f \;\; \frac{1}{2}f_s - f_f]$, where f_f is the fault characteristic frequency which can be calculated using the equation (13), given in the next section and f_s is the sampling frequency of the vibration signal.

Step 3: In this step, the initial position and velocity vectors are generated for the whole swarm size. The size of each position and velocity matrix is $D \times m$. The values of the initial swarm are random and within the bound limits such as:

$$s_{lb} \leqslant s_{md} \leqslant s_{ub}\,, \tag{12}$$

where s_{lb} and s_{ub} are the lower bound and upper bound of the swarm and s_{md} is the generated particle.

After generating the initial swarm, the fitness value of each potential solution is calculated using the proposed fitness function described above. The initial p_{best} is determined using the fitness values of each potential solution where the potential solution with the maximum fitness value represents the initial g_{best}.

Step 4: In step 4, p_{best} and g_{best} are updated. For that, the initial or previous p_{best} is compared with the current p_{best} evaluated by the updated swarm. The maximum fitness value of the resultant p_{best} represents the current g_{best} which is compared to the previous g_{best} to determine the resultant g_{best} in each epoch.

Step 5: In step 5, the position and velocity vectors are updated using the equation (11). The updated position and velocity must be within the bound limits according to the equation (12).

Step 6: In the final step, the optimized value among the G_{best} vector is determined. This g_{best} value corresponds to the maximum fitness value and determines the optimized parameters for the proposed Morlet wavelet filter for the faulty vibration signal.

5. Simulations and results

The Machinery Failure Prevention Technology (MFPT) data set is used as a benchmark to perform the simulations and verify the performance of the proposed the ARL-wavelet-BPF. The MFPT data set consists of different vibration signals with baseline conditions, inner race fault conditions, and outer race fault conditions. The data set was recorded at various loads and can be accessed from their website [1]. To record the data set, the test rig was equipped with a NICE bearing with the following parameters:

- Roller diameter: $d = 0.235$.
- Pitch diameter: $D = 1.245$.
- Number of elements: $n = 8$.
- Contact angle: $\alpha = 0$.

Fault frequencies in rotary bearings can be classified as (1) outer race ball pass fault frequency (BPFO), (2) inner race ball pass fault frequency (BPFI), (3) fundamental train fault frequency (FTF), and (4) fault frequency due to ball spin (BSF) [17]. All these fault frequencies can be calculated using the bearing specification that includes the number of rolling elements in the bearing (n), the diameter of the rolling elements (d), the pitch diameter of the bearing (D), the bearing contact angle (α), and the shaft frequency (f_s). The formulae to calculate these faults frequencies using the selected bearing specifications are given below [8, 16, 17]:

$$\begin{aligned} BPFO &= 0.5nf_1\left(1-\frac{d\cos(\alpha)}{D}\right),\\ BPFI &= 0.5nf_1\left(1+\frac{d\cos(\alpha)}{D}\right),\\ FTF &= 0.5f_1\left(1-\frac{d\cos(\alpha)}{D}\right),\\ BSF &= \frac{0.5D}{d}\left(1-\left(\frac{d\cos(\alpha)}{D}\right)^2\right). \end{aligned} \tag{13}$$

In this paper, two data files with outer race fault conditions and two data files with baseline conditions are considered. These data files have a low signal-to-noise ratio and their fault frequencies are not visualized using frequency-domain representation such as envelope spectrum. Each of these vibration signals is recorded for 6 seconds with 270 lbs of load, an input shaft rate of 25 Hz, and a sampling rate of 97,656 samples per second (sps).

Following is the time-dome representation of the first vibration signal with outer race fault. Fig. 2a shows the original signal and Fig. 2b shows the filtered vibration signal. The envelope spectrum of both time-domain signals is shown in Fig. 2c and Fig. 2d, respectively. It can be observed from Fig. 2d that the signal-to-noise ratio is high and periodic outer race fault conditions are prominent.

Similar to the first vibration signal, the second vibration signal is shown in Fig. 3. The results from Fig. 2d and Fig. 3d verify the performance of the proposed filtration method.

Next, two more vibration signals with baseline conditions are considered. These vibration signal also have a low signal-to-noise ratio and their envelope spectrum do not visualize the fault frequency. When the proposed ARL-wavelet-BPF is applied to these faulty signals, the signal-to-noise ratio is improved and baseline conditions can be visualized. The first vibration signal with baseline condition is shown in Fig. 4. Fig. 4a and 4b show the original time-domain signal and filtered time-domain vibration signal, respectively. The envelope spectrum of both vibration signals is shown in Fig. 4cand 4d, respectively.

Similarly, the second vibration signal with baseline condition is shown in Fig. 5. Fig. 5a, 5b, 5c, and 5d show the time-domain vibration signal, filtered vibration signal in the time-domain, envelope spectrum of the unfiltered signal, and envelope spectrum of the filtered vibration signal, respectively. The results from these experiments show the performance of the proposed method and indicate that the proposed method is efficient for faulty vibration signals with a low signal-to-noise ratio (SNR).

Furthermore, SNR is also calculated for all the experiments for quantitative comparison. Table 2 shows the relationship between SNR for unfiltered signals and filtered signals. For the filtered signal, SNR is calculated using the following formula:

$$\mathrm{SNR}_{\text{filtered signal}} = \frac{\sum_{n=1}^{s} \max_{n \in V_{\text{peaks}}} (ES_f[n]^2)/s}{\sum_{n=1}^{l} ES_s[n]^2/l}, \tag{14}$$

where s is the number of spikes in the envelope spectrum of the filtered signal that is taken to compute the SNR, V_{peaks} is a vector containing all the spikes, $ES_f[n]$ is the envelope spectrum of the filtered signal. l is the number of spikes in the envelope spectrum of the unfiltered signal, and $ES_s[n]$ is the envelope spectrum of the unfiltered signal. Note that we have considered the whole unfiltered vibration signal to calculate the SNR, hence, l is equal to the total number of samples in the envelope spectrum of the unfiltered vibration signal.

To calculate the SNR for an unfiltered signal, the same number of spikes are taken from the envelope spectrum of the vibration signal with the same position

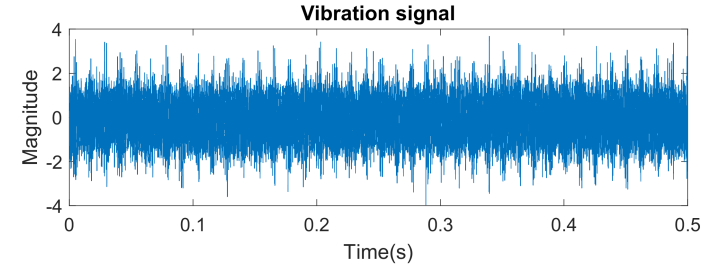

(a)

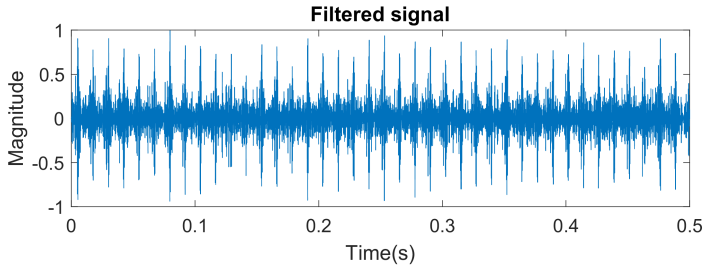

(b)

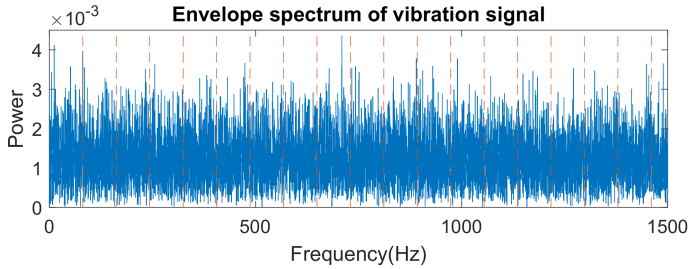

(c)

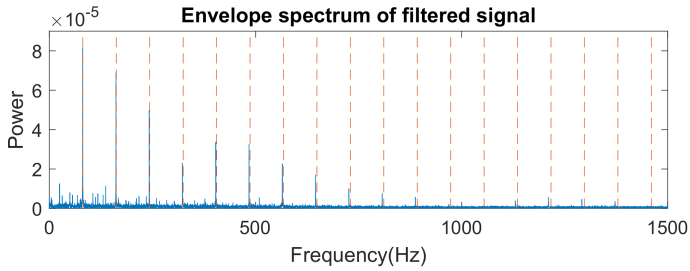

(d)

Figure 2: First vibration signal with outer race fault: a) time plot of the unfiltered signal, b) time plot of the filtered signal, c) envelope spectrum of the unfiltered signal, d) envelope spectrum of the filtered signal

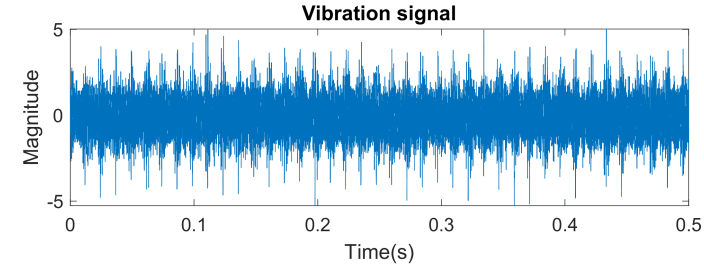

(a)

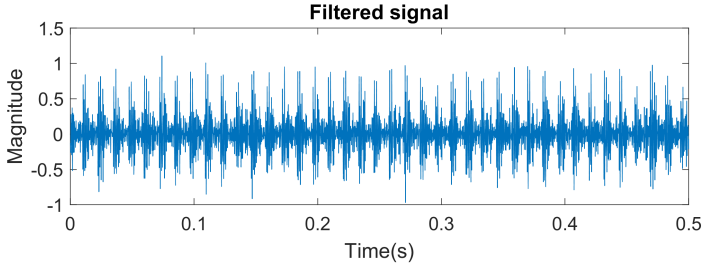

(b)

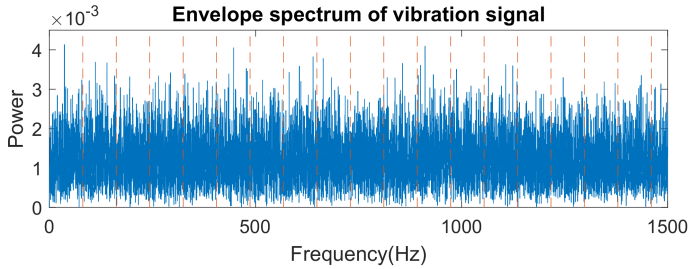

(c)

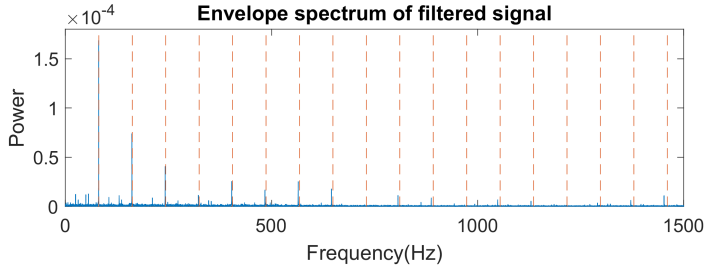

(d)

Figure 3: Second vibration signal with outer race fault: a) time plot of the unfiltered signal, b) time plot of the filtered signal, c) envelope spectrum of the unfiltered signal, d) envelope spectrum of the filtered signal

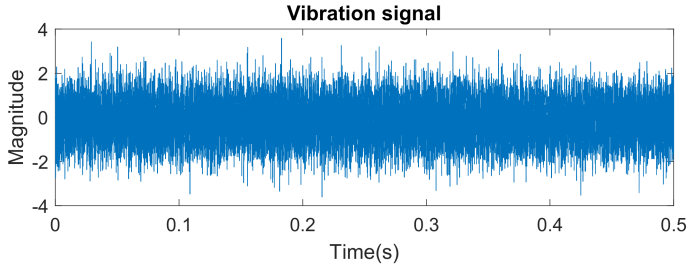

(a)

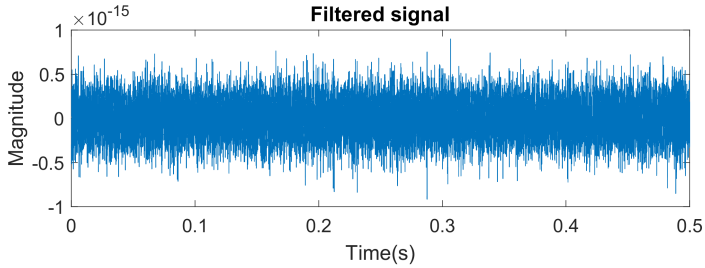

(b)

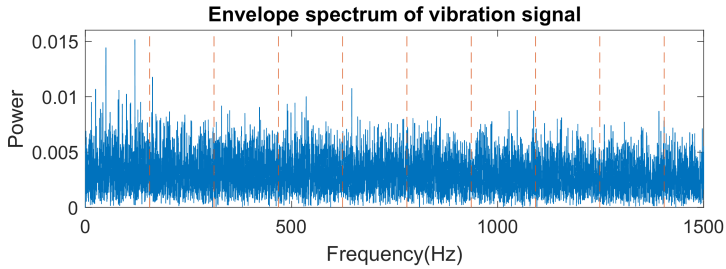

(c)

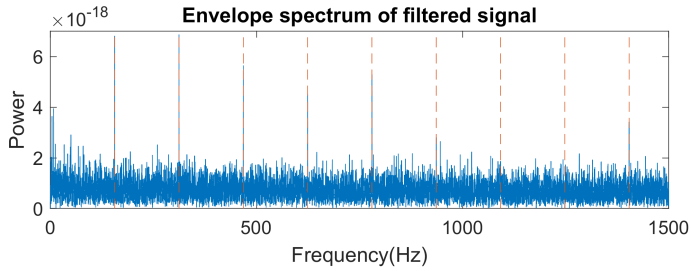

(d)

Figure 4: First vibration signal with baseline condition: a) time plot of the unfiltered signal, b) time plot of the filtered signal, c) envelope spectrum of the unfiltered signal, d) envelope spectrum of the filtered signal

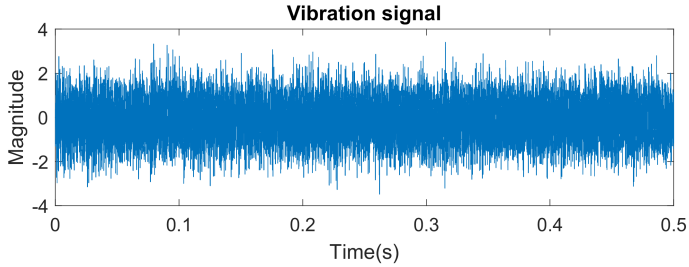

(a)

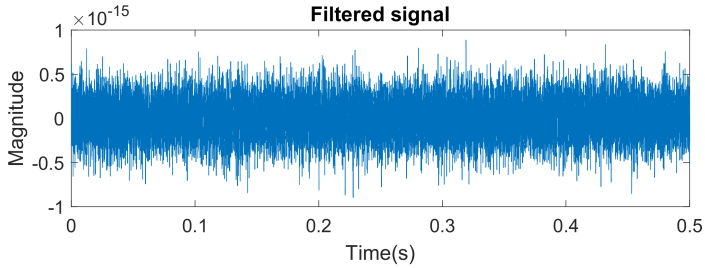

(b)

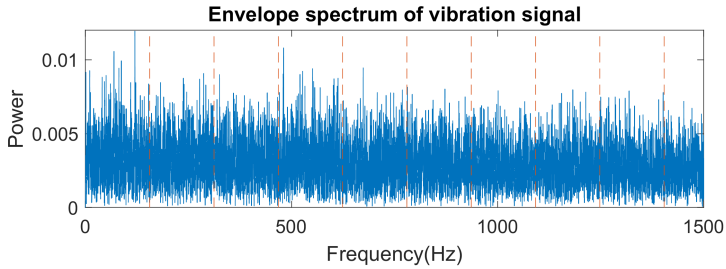

(c)

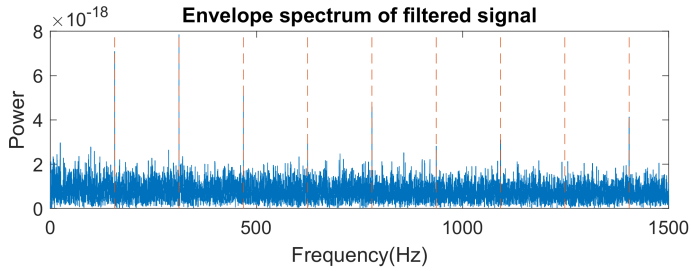

(d)

Figure 5: Second vibration signal with roller element fault: a) time plot of the vibration signal, b) time plot of the filtered vibration signal, c) envelope spectrum of the vibration signal, d) envelope spectrum of the filtered vibration signal

Table 2: Quantitative comparison of SNR

Experiment	$\text{SNR}_{\text{unfiltered signal}}$	$\text{SNR}_{\text{filtered signal}}$	SNR_{db_u}	SNR_{db_f}
1	4.4814	96.3686	6.5141	19.8394
2	3.7846	155.2415	5.7802	21.9101
3	2.9334	19.1820	4.6737	12.8289
4	1.9944	19.9933	2.9982	13.0089

as the envelope spectrum of the filtered signal. To visualize the chosen spikes from the envelope spectrum, we will consider the first experiment again. Fig. 6a shows the taken spikes from the envelope spectrum of the filtered signal which was computed for the first experiment with outer race fault and given in Fig. 2d. To compute the SNR for the unfiltered signal, the spikes were taken from the same position which is depicted in Fig. 6b. Similar to the above, other signals were processed in the same way to find the spikes for SNR. Furthermore, Table 2 shows that the proposed method is efficient to enhance the SNR and hence effective to determine the fault conditions for the vibration signals having high noise.

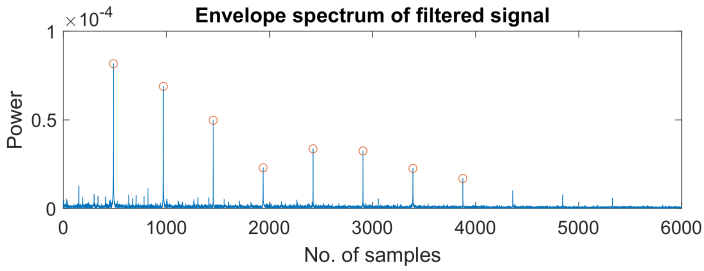

(a)

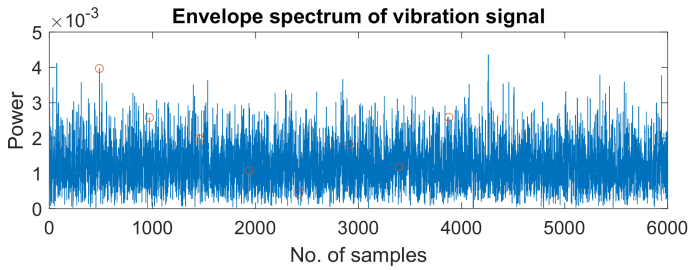

(b)

Figure 6: Envelope spectrum of the outer race fault condition: a) spikes from the filtered signal, b) spikes from the unfiltered signal

6. Conclusion

This paper proposes a new method to enhance the signal-to-noise ratio by applying the ARL-wavelet-BPF to diagnose the fault frequencies in bearing vibration signals. The Gaussian function of the ARL-wavelet used in this paper is an excellent BPF because of its smooth edges which helps to minimize the ripple effects. The ARL-wavelet is symmetric in its geometric shape and hence can diagnose the vibration fault more efficiently compared to other wavelets such as the Morlet wavelet. Furthermore, the PSO algorithm is used to optimize the filter parameters such as the bandwidth and center frequency. From the experimental results, it is concluded that the proposed method enhances the signal-to-noise ratio and detects the fault frequencies efficiently.

References

[1] Mfpt dataset. *Society for Machinery Failure Prevention Technology*, 2012.

[2] M. Ahsan and D. Bismor: Early-stage fault diagnosis for rotating element bearing using improved harmony search algorithm with different fitness functions. *IEEE Transactions on Instrumentation and Measurement*, **71** (2022). DOI: 10.1109/TIM.2022.3192254.

[3] M. Ahsan and D. Bismor: Early-stage faults detection using harmony search algorithm and stft-based spectral kurtosis. In Roman Szewczyk, Cezary Zieliński, and Małgorzata Kaliczyńska (eds.), *Automation 2022: New Solutions and Technologies for Automation, Robotics and Measurement Techniques*, 2022, 75–84, Cham, Springer International Publishing. DOI: 10.1007/978-3-031-03502-9_8.

[4] J. Antoni: The spectral kurtosis: A useful tool for characterising non-stationary signals. *Mechanical Systems and Signal Processing*, **20**(2), (2006), 282–307. DOI: 10.1016/j.ymssp.2004.09.001.

[5] J. Antoni: Fast computation of the kurtogram for the detection of transient faults. *Mechanical Systems and Signal Processing*, **21**(1), (2007), 108–124. DOI: 10.1016/j.ymssp.2005.12.002.

[6] J. Antoni and R.B. Randall: The spectral kurtosis: Application to the vibratory surveillance and diagnostics of rotating machines. *Mechanical Systems and Signal Processing*, **20**(2), (2006), 308–331. DOI: 10.1016/j.ymssp.2004.09.002.

[7] D. Bismor: Analysis and comparison of vibration signals from internal combustion engine acquired using piezoelectric and MEMS accelerometers. *Vibration in Physical Systems*, **30**(1), (2019). https://vibsys.put.poznan.pl/_journal/2019-30-1/vibsys_2019-vol30-1-book.pdf.

[8] D. Bismor: System for vehicle sound and vibration monitoring using mems sensors. *2019 Signal Processing: Algorithms, Architectures, Arrangements, and Applications (SPA)*, Poznan, Poland, (2019). DOI: 10.23919/SPA.2019.8936824.

[9] K. Gao, Z. Cao, L. Zhang, Z. Chen, Y. Han and Q. Pan: A review on swarm intelligence and evolutionary algorithms for solving flexible job shop scheduling problems. *IEEE/CAA Journal of Automatica Sinica*, **6**(4), (2019), 904–916. DOI: 10.1109/JAS.2019.1911540.

[10] X. Gu, S. Yang, Y. Liu and R. Hao: Rolling element bearing faults diagnosis based on kurtogram and frequency domain correlated kurtosis. *Measurement Science and Technology*, **27**(12), (2016), 125019. DOI: 10.1088/0957-0233/27/12/125019.

[11] Y. Hu, W. Bao, X. Tu, F. Li and nd K. Li: An adaptive spectral kurtosis method and its application to fault detection of rolling element bearings. *IEEE Transactions on Instrumentation and Measurement*, **69**(3), (2020), 739–750. DOI: 10.1109/TIM.2019.2905022.

[12] K. Jianshe, X. Lei, Z. Jianmin and T. Hongzhi: A new improved kurtogram and its application to bearing fault diagnosis. *Shock and Vibration*, **2015**(3), (2015), 1–22. DOI: 10.1155/2015/385412.

[13] D. Krokavec, A. Filasová and P. Liščinský: On fault tolerant control structures incorporating fault estimation. *Archives of Control Sciences*, **26**(4), (2016), 453–469. DOI: 10.1515/acsc-2016-0025.

[14] Y. Lei, J. Lin, Z. He and Y. Zi: Application of an improved kurtogram method for fault diagnosis of rolling element bearings. *Mechanical Systems and Signal Processing*, **25**(5), (2011), 1738–1749. DOI: 10.1016/j.ymssp.2010.12.011.

[15] A. Pries, D. Ramírez and P.J. Schreier: LMPIT-inspired tests for detecting a cyclostationary signal in noise with spatio-temporal structure. *IEEE Transactions on Wireless Communications*, **17**(9), (2018), 6321–6334. DOI: 10.1109/TWC.2018.2859314.

[16] A. Rai and S.H. Upadhyay: A review on signal processing techniques utilized in the fault diagnosis of rolling element bearings. *Tribology International*, **96** (2016), 289–306. DOI: 10.1016/j.triboint.2015.12.037.

[17] R.B. Randall and J. Antoni: Rolling element bearing diagnostics – A tutorial. *Mechanical Systems and Signal Processing*, **25**(2), (2011), 485–520. DOI: 10.1016/j.ymssp.2010.07.017.

[18] M. Rhif, A. Ben Abbes, I. Riadh Farah, B. Martínez and Y. Sang: Wavelet transform application for/in non-stationary time-series analysis: A review. *Applied Sciences*, **9**(7), (2019). DOI: 10.3390/app9071345.

[19] J. Stolarek: Improving energy compaction of a wavelet transform using genetic algorithm and fast neural network. *Archives of Control Sciences*, **20**(4), 2010, 417–433.

[20] R.-B. Sun, F.-P. Du, Z.-B. Yang, X.-F. Chen and K. Gryllias: Cyclostationary analysis of irregular statistical cyclicity and extraction of rotating speed for bearing diagnostics with speed fluctuations. *IEEE Transactions on Instrumentation and Measurement*, **70** (2021), 1–11. DOI: 10.1109/TIM.2021.3069381.

[21] M.-Q. Tran, M.-K. Liu, Q.-V. Tran and T.-K. Nguyen: Effective fault diagnosis based on wavelet and convolutional attention neural network for induction motors. *IEEE Transactions on Instrumentation and Measurement*, **71** (2022), 1–13. DOI: 10.1109/TIM.2021.3139706.

[22] S.S. Udmale and S. Kumar Singh: Application of spectral kurtosis and improved extreme learning machine for bearing fault classification. *IEEE Transactions on Instrumentation and Measurement*, **68**(11), (2019), 4222–4233. DOI: 10.1109/TIM.2018.2890329.

[23] D. Wang, P.W. Tse and K. Leung Tsui: An enhanced kurtogram method for fault diagnosis of rolling element bearings. *Mechanical Systems and Signal Processing*, **35**(1), (2013), 176–199. DOI: 10.1016/j.ymssp.2012.10.003.

[24] X. Wang, B. Wang and W. Chen: The second-order synchrosqueezing continuous wavelet transform and its application in the high-speed-train induced seismic signal. *IEEE Geoscience and Remote Sensing Letters*, **18**(6), (2021), 1109–1113. DOI: 10.1109/LGRS.2020.2993596.

[25] X. Xia, Y. Xing, B. Wei, Y. Zhang, X. Li, X. Deng and L. Gui: A fitness-based multi-role particle swarm optimization. *Swarm and Evolutionary Computation*, **44** (2019), 349–364. DOI: 10.1016/j.swevo.2018.04.006.